Earth and Planetary Science Letters 351–352 (2012) 195–207

Contents lists available at SciVerse ScienceDirect

Earth and Planetary Science Letters

journal homepage: www.elsevier.com/locate/epsl

The mobility of W and Mo in subduction zone fluids and the Mo–W–Th–U systematics of island arc magmas

E. Bali [a,b,*], H. Keppler [b], A. Audetat [b]

[a] Department of Experimental and Applied Mineralogy, Georg-August University, 37077 Göttingen, Germany
[b] Bayerisches Geoinstitut, University of Bayreuth, 95440 Bayreuth, Germany

ARTICLE INFO

Article history:
Received 16 February 2012
Received in revised form
18 July 2012
Accepted 19 July 2012
Editor: T. Elliot
Available online 31 August 2012

Keywords:
oxygen fugacity
fluid salinity
subduction zones
W-solubility
Mo-solubility

ABSTRACT

We have studied the solubility of W- and Mo-oxide in aqueous fluids at 2.61 GPa, 600 to 800 °C at variable controlled oxygen fugacity conditions, relevant to subduction zones. We observed that the solubility of W-oxide is only slightly dependent on fO_2 between conditions buffered by Co–CoO and Re–ReO_2. In contrast, Mo-oxide solubility is strongly dependent on both oxygen fugacity and fluid salinity under the same conditions. At 2.61 GPa, in the fO_2 range between Co–CoO and Re–ReO_2 their solubility can be described by the following equations:

$$\log W = 0.07 \log fO_2 - 4.72 \times 1000/T + 4.43$$

and

$$\log Mo = 0.44 \log fO_2 + 0.42 \log NaCl - 1.8 \times 1000/T + 4.80$$

where W, Mo and NaCl are concentrations in molalities, fO_2 is oxygen fugacity and T is temperature in Kelvin. We also studied the solubility of Mo and W in mantle minerals coexisting with Mo- and W-oxide and combined these data with the fluid solubilities to calculate fluid/mineral partition coefficients of W and Mo. Both W and Mo are incompatible in the structure of major eclogite minerals (garnet and clinopyroxene) in the presence of aqueous fluid, but they are compatible in rutile. Thus, the presence or absence of rutile strongly affects the mobility of these elements in subduction zones. From the partition coefficients we calculated the composition of aqueous fluid released from an N-MORB eclogite source. We found that the Mo–Ce–W–Th–U systematics of arc magmas can be modeled by the mixing of depleted mantle with an aqueous fluid phase that was released from a rutile-bearing N-MORB source in fO_2-conditions between FMQ-1.6 and FMQ+3 having a maximum salinity of 20 wt% $NaCl_{equiv}$. If rutile contents in residual eclogite are independently determined, redox conditions, salinity and amount of fluid added to the source region of melting can be tightly constrained by plotting Mo/Ce, W/Th, and Mo/W vs. U/Th. In particular, the W/Th ratio is a sensitive indicator of the amount of fluid, since W always very strongly partitions into the fluid, nearly independent of oxygen fugacity and salinity. The Mo/W ratio is particularly sensitive to redox conditions, while U/Th reflects both salinity and redox state.

1. Introduction

The behavior of tungsten and molybdenum varies in different geochemical environments. In the presence of metallic iron they are siderophile, thus e.g. $^{182}W/^{184}W$ isotopic ratios have been used for dating the differentiation of planetary bodies (e.g., Jacobsen and Harper, 1995; Lee and Halliday, 1995). During mantle melting, however, they are highly incompatible (e.g., Adam and Green, 2006), leaving a depleted mantle behind and producing a relatively tungsten- and molybdenum-rich crust (2.4 ppb vs. 1 ppm for W and 25 ppb vs. 1.1 ppm for Mo, Salters and Stracke, 2004; Rudnick and Gao, 2004, König et al., 2011). Moreover, the existence of hydrothermal tungsten- and molybdenum-ore deposits suggests that they should be mobile in aqueous fluid.

Noll et al. (1996) have systematically studied the abundance of siderophile elements in subduction related magmas. They concluded that W, Mo and Sn are immobile in subduction zone fluids, whereas other elements such as As, Pb or Sb should be strongly mobile. Recently, König et al. (2008, 2010, 2011) have carried out

* Corresponding author at: Department of Experimental and Applied Mineralogy, Georg-August University, 37077 Göttingen, Germany.
Tel.: +49 551 39 3864; fax: +49 551 39 3863.
E-mail address: ebali@gwdg.de (E. Bali).

0012-821X/$ - see front matter © 2012 Elsevier B.V. All rights reserved.
http://dx.doi.org/10.1016/j.epsl.2012.07.032

high-precision W-analyses on different sets of subduction related lavas. In contrast to Noll et al. (1996), they found that tungsten, and also molybdenum, can be mobilized by subduction zone fluids, although their relative enrichment can be decoupled. They observed that e.g. in Solomon arc lavas the enrichment of W and Mo was positively correlated, whereas in Cyprus boninites W was significantly enriched and Mo was depleted relative to the other fluid mobile elements. They speculated that the decoupling may be caused by (1) initially different Mo/W ratios in the subduction component; (2) the presence or absence of residual sulfides in the source region of arc magmas that might sequester Mo but not W during mantle melting; or (3) the different redox-sensitivity and salinity dependence of W and Mo mobility in aqueous fluids.

In this paper we explore the third scenario in detail. Rather than directly measuring fluid/mineral partition coefficients, we separately determined the solubilities of Mo- and W-oxide in aqueous fluids and in minerals and calculated fluid/melt partition coefficients from these data. This procedure has the advantage that equilibrium between the fluid and the saturating oxide is easily reached by simple dissolution of the oxide, while in experiments that attempt to measure fluid/mineral partition coefficients directly, the very low diffusion rates of trace elements in the crystal lattice of silicates can make attainment of equilibrium difficult or impossible. We carried out W- and Mo-oxide solubility experiments at 2.61 GPa, 600 to 800 °C at variable controlled oxygen fugacity conditions. These pressure and temperature conditions are close to amphibole dehydration in subduction zones. The W- or Mo- saturated fluid was trapped as synthetic fluid inclusions in quartz and analyzed subsequently by LA-ICPMS. Furthermore, we determined the maximum solubility of these elements in eclogite minerals (diopside, garnet and rutile) also at variable oxygen fugacities in order to check if oxygen fugacity has any effect on the incorporation mechanism of Mo and W. For both elements, we calculated fluid/mineral partition coefficients for an eclogitic mineral assemblage. Combining these data with those from the U- and Th-study of Bali et al. (2011) we built a comprehensive model to explain the Mo–Ce–W–U–Th systematics of island arc magmas to infer the redox state, the salinity and the amount of fluid added to the region of melting.

These new results might have further implication for the global mass balance of W as discussed extensively by König et al. (2011) and references therein.

2. Experimental procedure and analytical techniques

Here we present briefly the experimental and analytical procedures. Detailed description of experimental techniques is in Appendix A.

2.1. Starting materials and capsule preparation

Synthetic fluid inclusions were trapped in natural, inclusion-free quartz from Brazil. For each experiment, a quartz piece was loaded into a $Pt_{95}Rh_{05}$ capsule together with powder of high purity WO_2 or MoO_3 and fluid (Table 1). The stoichiometry of the saturating Mo or W oxide was controlled by the equilibrium with the external buffer during the experiment. The aqueous fluid used for the MoO_3-bearing experiments had a salinity of 0.39 to 14.1 wt% $NaCl_{equiv}$. It was spiked with 860–998 ppm Cs, Rb and Ba, added as chlorides, to provide internal standards for LA-ICPMS analysis. The aqueous fluid used for the WO_2-bearing experiments contained variable amount of NaCl. The fluid salinity varied from 2.0 to 20.0 wt% $NaCl_{equiv}$. Oxygen fugacity was controlled by external Fe–FeO, Co–CoO, Ni–NiO and Re–ReO_2 buffers (Table 1).

We also determined the partitioning of W and Mo between aqueous fluid and major eclogite and peridotite minerals. For this, the solubility of W and Mo in diopside, garnet, and rutile was studied at variable fO_2 conditions, using CMAS- or CMASTi-oxide powder, fluid and the same WO_2 and MoO_3 powder was used in the synthetic fluid inclusion experiments (Table 2). The experiments were buffered by Co–CoO, Ni–NiO and Re–ReO_2, and the fluid was pure water (Table 2). Two experiments have been carried out in W-undersaturated conditions in order to check if

Table 1
Experimental details and results of synthetic fluid inclusion experiments. Runs indicated by * are $CaWO_4$-solubility experiments.

Sample no.	Buffer	T (°C)	Capsule	Weight of starting material(g)			$NaCl_{eqiuv}$ in loaded fluid (wt%)	No. of analyzed inclusions	Average concentration (ppm)	1 δ st dev (%)
				Qz	WO_2/MoO_3	Fluid				
W05	Ni–NiO	800	outer: Ni, inner: Pt/Rh	0.02587	0.00966	0.02703	14.1	8	23026	3
W11	Ni–NiO	800	outer: Ni, inner: Pt/Rh	0.02449	0.01208	0.02520	2.0	7	27860	6
W12	Ni–NiO	800	outer: Ni, inner: Pt/Rh	0.02471	0.01235	0.02564	10.0	9	22891	5
W13	NiNiO	800	outer: Ni, inner: Pt/Rh	0.02638	0.01026	0.02690	20.0	11	22245	6
W14	Ni–NiO	800	outer: Ni, inner: Pt/Rh	0.02797	0.00679	0.02320	5.0	8	26370	7
W15	Re–ReO_2	800	outer: Pt/Rh, inner: Pt/Rh	0.03146	0.01141	0.01976	5.0	9	36178	8
W16	Co–CoO	800	outer: Co, inner: Pt/Rh	0.02042	0.00940	0.02408	5.0	11	18494	7
W17	Fe–FeO	800	outer: Fe, inner: Pt/Rh	0.03282	0.00749	0.01917	5.0	9	2987	10
W18	Ni–NiO	600	outer: Ni, inner: Pt/Rh	0.01893	0.00535	0.02779	5.0	12(pr:4 s:8)	2630	20
W19	Ni–NiO	700	outer: Ni, inner: Pt/Rh	0.01874	0.00523	0.02626	5.0	9(2; 7)	9980	7
W22	Co–CoO	800	outer: Co, inner: Pt/Rh	0.02680	0.01293*	0.02102	5.0	8	13125	10
W23	Re–ReO_2	800	outer: Pt/Rh, inner: Pt/Rh	0.02739	0.01479*	0.01886	5.0	7	18673	16
Mo02	Co–CoO	800	outer: Co, inner: Pt/Rh	0.02384	0.01367	0.02187	5.0	7	165	38
Mo03	Re–ReO_2	800	outer: Pt/Rh, inner: Pt/Rh	0.19320	0.01281	0.02623	5.0	5	4875	16
Mo05	Ni–NiO	800	outer: Ni, inner: Pt/Rh	0.02285	0.01020	0.02435	5.0	10	290	28
Mo06	Ni–NiO	700	outer: Ni, inner: Pt/Rh	0.03269	0.01042	0.02149	5.0	7	193	14
Mo07	Ni–NiO	600	outer: Ni, inner: Pt/Rh	0.02836	0.01054	0.02244	5.0	7	164	17
Mo08	Ni–NiO	800	outer: Ni, inner: Pt/Rh	0.23390	0.00651	0.02493	14.1	8	735	20
Mo11	Ni–NiO	800	outer: Ni, inner: Pt/Rh	0.01860	0.00660	0.02190	0.40	143	143	35
Mo13	Ni–NiO	800	outer: Ni, inner: Pt/Rh	0.02024	0.01306	0.01364	0.4+5 wt% HCl	4	107	47

Table 2
Composition of run products and starting materials from experiments on Mo and W solubility in mantle minerals where clear signals were detected below the nominal detection limit of LA-ICPMS analyses, concentrations were calculated and numbers are given in parenthesis.

	Clinopyroxene											
	Mo09 Co–CoO $n=8$	range	**Mo10** Ni–NiO $n=6$	range	**Mo14** Ni–NiO $n=5$	range	**W24** Co–CoO $n=3$	range	**W25** Re–ReO_2 $n=9$	range	**W27–W28** Ni–NiO $n=10$	range
SiO_2	53.3	52.5–54.3	54.7	53.7–55.6	53.6	53.4–53.9	55.7	55.2–56.0	54.9	53.6–55.4	52.56	51.2–53.4
Al_2O_3	4.30	1.9–9.7	2.20	1.38–3.16	3.20	2.61.3.49	2.51	2.19–2.94	2.04	1.46–3.74	4.23	3.40–5.48
TiO_2	–	–	–	–	0.50	0.42–0.73	–	–	–	–	0.88	0.63–1.14
MgO	17.9	17.8–19.3	18.3	17.4–19.2	17.9	17.5–18.5	20.0	19.1–20.7	19.0	18.7–19.4	17.76	17.2–18.4
CaO	25.1	23.8–26.2	25.0	24.4–25.6	24.3	24.0–24.8	21.8	20.9–22.8	24.2	23.8–24.6	24.45	24.3–24.6
WO_3	–	–	–	–	–	–	b.d.	–	b.d.	–	b.d.	–
MoO_3	b.d.	–	b.d.	–	b.d.	–	–	–	–	–	–	–
total	100.6		100.2		99.6		99.9		100.2		99.9	
Mo (ppm)	34.0	18–46	46	26–64	118	89–162	–	–	–	–	–	–
W (ppm)	–	–	–	–	–	–	70	55–90	55	37–83	<20 (6.5) <22 (1.5)[b]	(6–7) (0–3)
Added H_2O (wt%)	22		20		14		28		22		26/22	
	Garnet											
	Mo09 Co–CoO grt core ($n=3$)[a]	range	grt rim	**Mo14** Ni–NiO grt core ($n=3$)		**W24** Co–CoO grt core[a]	grt rim	**W25** Re–ReO_2 grt core ($n=3$)[a]	range	grt rim ($n=2$)	range	**W27-28** Ni–NiO grt ($n=5$)	range
SiO_2	44.6	43.7–46.3	46.1	44.0	43.2–44.6	43.6	43.9	44.8	44.6–45.7	44.3	44.0–44.5	42.7	42.5–42.8
Al_2O_3	24.5	23.3–25.1	19.2	20.0	17.7–23.5	25.3	25.1	23.2	21.9–24.7	25.2	25.1–25.4	23.4	23.0–23.7
TiO_2	–		–	1.35	0.63–2.16	–	–	–		–		0.94	0.91–0.97
MgO	23.3	23.2–23.4	21.1	21.6	20.9–22.7	24.5	25.0	23.0	22.5–23.6	25.6	25.4–25.7	21.3	21.2–21.4
CaO	8.83	8.50–9.10	13.8	12.1	8.93–14.5	6.51	6.00	10.1	8.99–11.1	6.29	6.18–6.55	11.2	11.1–11.4
WO_3	–	–	–	–	–	b.d.	b.d.	b.d.	–	b.d.	–	b.d.	–
MoO_3	b.d.	–	b.d.	b.d.	–	–	–	–	–	–	–	–	–
total	101.2		100.2	99.0		100.0	100	101.1		101.4		99.6	
Mo (ppm)	–		<10	<130(13)	(7–19)	–	–	–	–	–	–	–	–
W (ppm)	–	–	–	–	–	–	<20(6 (0–12))	–	–	<14(3)	(0.58–6.35)	<10(3.5)	(1–6)
	Rutile				**Forsterite**			**Spinel**		**CMAS starting powder**		**CMASTi starting powder**	
	Mo14 Ni–NiO n=5	range	**W27-28** Ni–NiO n=8	range	**Mo09** Co-CoO n=1	**W27-W28** Ni-NiO n=3	range	**Mo09** Co-CoO n=3	range				
SiO_2	0.08	0.03–0.10	0.15	0.02–0.84	42.9	41.7	41.3–42.1	0.12	0.10–0.15	53.02		44.77	
Al_2O_3	1.76	1.74–1.79	1.71	1.61–1.79	0.02	0.09	0.06–0.14	70.5	70.2–70.8	5.07		4.29	
TiO_2	83.8	82.5–85.3	95.8	94.3–94.6	–	0.51	0.32–1.00	–	–	–		15.19	
MgO	0.50	0.48–0.51	0.55	0.51–0.67	57.5	56.3	55.3–56.9	28.2	28.1–28.2	17.81		15.07	
CaO	0.45	0.01–0.67	0.59	0.09–1.50	0.05	0.23	0.11–0.38	0.04	0.02–0.06	24.10		20.68	
WO_3	–	–	0.55	0.43–0.65	–	b.d.	–						
MoO_3	13.2	12.0–14.2	–	–	b.d.	–	–						
total	99.8		99.3		100.5	98.8		98.8					
Mo (ppm)	14.67 wt%	–	–	–	–	–	–	<12	(0)				
W (ppm)	–	–	5465 5150[b]	4760–6040 3490–7360[b]	–	<20(6)	–	–	–				

[a] Too inclusion-rich to be analyzed by LA-ICPMS.
[b] Analyzed in W28.

the partitioning of W is constant even if the W-content of the fluid is an order of magnitude less than in saturated conditions.

2.2. High pressure experiments

The experiments were carried out in an end-loaded piston cylinder apparatus at the Bayerisches Geoinstitut, Bayreuth and at the Department of Experimental and Applied Mineralogy, University of Göttingen. In both cases we used 1/2 in. MgO–NaCl assemblies, with stepped graphite heaters. The temperature was measured by Pt/Pt–Rh ("S-type") thermocouple and monitored by a Eurotherm controller.

Synthetic fluid inclusion experiments were carried out at temperatures of 600 to 800 °C at a constant pressure of 2.61 GPa (Table 1). Fluid pH is not explicitly buffered in these experiments. Experimental duration was 1 day. The Mo and W solubility experiments in mantle silicates and rutile were 48 to 72 h long.

2.3. Analytical techniques

Quartz pieces from synthetic fluid inclusion experiments were doubly polished. For analysis we selected fluid inclusions which did not show any decrepitation phenomena and did not contain optically visible, accidentally trapped solid W-oxide or Mo-oxide (e.g. Fig. 1a). Fluid inclusion analyses were carried out with an Elan quadrupole mass spectrometer (PerkinElmer) attached to a Geolas M 193 nm ArF ecximer laser (Coherent) at the Bayerisches Geoinstitut, Bayreuth. NIST SRM 610 glass was used as an external standard. Helium and in some of the measurements helium-hydrogene mixture was used as a carrier gas in the sample chamber. A He-gas flow of 0.4 l/min was coupled with a H_2 gas flow of 5 ml/min. The addition of H_2-gas has increased the sensitivity of the instrument for most of the analyzed elements (Guillong and Heinrich, 2007). Isotopes of ^{23}Na, ^{29}Si, ^{85}Rb, ^{133}Cs, ^{59}Co, ^{35}Cl, ^{184}W or ^{97}Mo and ^{98}Mo were analyzed in all run products. ^{57}Fe, ^{60}Ni or ^{185}Re were additionally analyzed in the

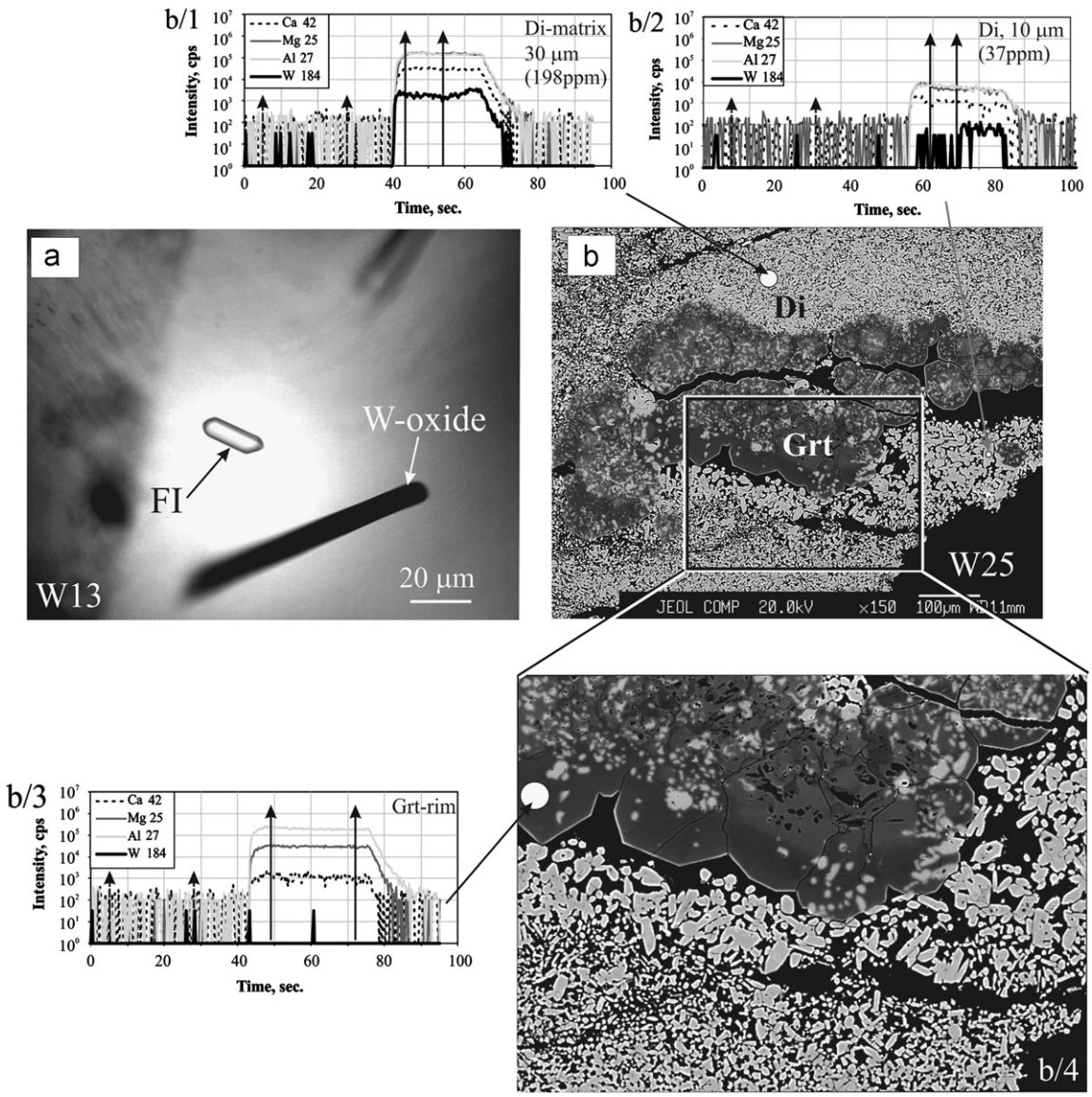

Fig. 1. Photomicrographs of run products. (a) Negative crystal shaped fluid inclusion (FI) and a $Na_{0.16}WO_3$ needle in quartz from run W13. The fluid contains 20.0 wt% $NaCl_{equiv}$ and was trapped at 2.61 GPa and 800 °C in equilibrium with NiNiO buffer. (b) Back scattered electron image of sample W25, containing diopside and garnet (2.61 GPa, 1000 °C, Re–ReO_2-buffer). In Figure b/4, note the bright 1–2 µm wide W-rich zone on garnet and matrix diopside rims. This bright zone is missing from inclusion diopsides. White dots indicate the sites of La-ICP-MS analyses. Respective schematic LA-ICPMS spectra are also shown. Signals were always integrated between the arrows. Signal b/2 shows an analysis where W-rich grain boundary contamination was reached at ~15 s after the start of ablation.

Table 3
Composition of W-oxides recovered from synthetic fluid inclusion experiments.

	W11 (Ni–NiO; 2 wt%)		**W12 (Ni–NiO; 10 wt%)**		**W13 (Ni–NiO; 20 wt%)**	
	Average of 33	1 δ st dev (%)	Average of 31	1 δ st dev (%)	Average of 7	1 δ st dev (%)
Na_2O	0.22	**153**	1.90	6	2.15	7
WO_3	96.9	1	93.5	1	93.4	2
total	97.1		95.4		95.6	
	W14 (NiNiO; 5 wt%)		**W15 ($ReReO_2$; 5 wt%)**		**W16 (CoCoO, 5 wt%)**	
	Average of 33	1 δ st dev (%)	Average of 31	1 δ st dev (%)	Average of 29	1 δ st dev (%)
Na_2O	1.71	4	0.27	**250**	1.52	7
WO_3	94.1	1	97.8	2	94.3	1
total	95.8		98.0		95.8	
	W18 (NiNiO; 5 wt%; 600 °C)		**W19 (NiNiO; 5 wt%; 700 °C)**			
	Average of 27	1 δ st dev (%)	Average of 25	1 δ st dev (%)		
Na_2O	1.72	3	1.70	4		
WO_3	94.5	1	93.7	1		
Total	96.2		95.4			

runs buffered by Fe–FeO, Ni–NiO and Re–ReO_2, respectively, to check for possible contamination of the fluid by these elements. No iron, rhenium or nickel contamination was observed. During the analyses the laser spot size was increased in several steps so as to pierce the inclusion first with a small beam (typically 6–10 μm), in order to avoid inclusion decrepitation, and finally ablating the whole inclusion volume.

For the Mo-oxide solubility experiments Rb and Cs were used as internal standards, whereas for the W-oxide solubility experiments we used Na. The reason for this was that in the fO_2-range between Co–CoO and Re–ReO_2 buffers W-oxide contained small amount of alkalies (Rb, Cs, Na) in solid solution. Rb/W and Cs/W ratios in both the fluid inclusions and the W-oxides were highly variable. Only the Na-content of the precipitated W-oxide compound and the Na/W ratio in fluid inclusions were found to be constant in one experimental charge (Table 3). Thus, we analyzed 30 random crystals from each experiment by EPMA (Table 3). Knowing the compositions of the precipitates and the exact amount of loaded WO_2, fluid as well as the fluid salinity, the Na-content of the equilibrium fluid was recalculated by mass balance and used for internal standardization. For experiments W11 and W15 the W-contents of the fluid (Table 1) can be considered as a minimum value, because the Na-contents of W-oxides in these experiments showed a much larger scatter (Table 2). Actually two populations of W-oxide were observed in both cases, one with higher Na_2O contents (~1.5 wt%) and one with no Na_2O. We recalculated the fluid composition assuming that all W-oxides had the higher Na_2O-content. In case of experiment W17 buffered by Fe–FeO, no recalculation was needed, as the recrystallized W-oxide did not incorporate any Na in its structure. In some inclusions clear Cl-signal was also observed. Cl-contents of these inclusions were calculated using a homogeneous afghanite (AfgAA) crystal (Seo et al., 2011) as an external standard and the recalculated Na-contents of the fluid as an internal standard. Calculated Cl-contents agreed with loaded Cl-contents with a precision of ±3% (1σ standard deviation).

Run products from studies of W and Mo solubilities in silicate minerals and rutile were mounted in epoxy and polished on one side. Mineral phases were identified by a Jeol Superprobe JXA-8200 at Bayerisches Geoinstitute, Bayreuth and by a Jeol Superprobe JXA-8900 at the Department of Geochemistry, University of Göttingen. Analyses were carried out with an accelerating voltage of 10 to 25 kV, a beam current of 20 nA and a beam size of 1–5 μm. Counting time for each element except Mo and W in rutile was 30 s. MoO_3 and WO_3 in rutiles were analyzed for 180 s. Natural and synthetic standards were used for calibration and a ZAF correction was applied. MoO_3 and WO_3 were calibrated by Mo- and W-metal standards provided by Jeol. LA-ICPMS analyses were carried out on the same instrument as for the fluid inclusions. Due to the generally small grain size, the beam diameter was 6–10 μm and the repetition rate was 3–5 Hz. The dwell time was 10 ms for Na^{23}, Mg^{25}, Al^{27}, Si^{29}, Ca^{42} and Ti^{49} but 30 ms for W^{184}, Mo^{97} and Mo^{98}. Mg was used as internal standard. Detection limits for both Mo and W were generally between 10 and 20 ppm (Table 2).

3. Results

3.1. Solubility of Mo and W in aqueous fluids

3.1.1. Fluid inclusions

A large number of primary fluid inclusions were trapped at 800 °C in quartz overgrowths within 24 h from the beginning of the experiments. They were generally rounded or negative crystal shaped and quenched to a homogeneous fluid phase (Fig. 1a). No daughter minerals of W- or Mo-oxide were observed in them, the occasionally occurring W- or Mo-oxide minerals in the inclusions were interpreted as accidental solid entrapment. The size of the inclusions reached 100 μm. In the experiments at lower temperatures fractured quartz was used. Small (up to 15 μm), rounded pseudosecondary inclusions were trapped in healed fractures. However, even at 600 °C sufficient quartz overgrowth (~100–150 μm) containing larger primary inclusions developed during the experiments. There was no difference among the compositions of primary and pseudosecondary inclusions in these run products indicating that equilibrium was reached very rapidly.

3.1.2. W- and Mo-oxides

Both W- and Mo-oxides recrystallized during the runs and the compositions changed according to the oxygen fugacity imposed by the external buffer. Both for Mo and W, an extensive series of mixed-valence oxides with compositions between WO_3/MoO_3 and WO_2/MoO_2 is known (e.g. Greenwood and Earnshaw, 1984). For tungsten oxides, there is in addition a solid solution series leading from pure WO_3 to the tungsten bronzes Na_xWO_{3-x} (e.g. Greenwood and Earnshaw, 1984; Labbe, 1992). W-oxide formed

brown cubic shaped crystals in the experiment buffered by Fe–FeO, purple-brown plates and needles in the experiments buffered by Co–CoO and Ni–NiO, and dark blue needles in the experiment buffered by Re–ReO_2. Mo-oxide recrystallized to violet needles in all run products, which shows that the originally loaded light blue MoO_3 recrystallized to MoO_2. The colors and crystal habit of the recrystallized W-oxides may be used to identify their crystal structure and the oxidation state of W in these compounds (e.g.: Labbe, 1992). In the experiments buffered by Fe–FeO, the brown cubic crystals correspond to WO_2. According to O'Neill and Pownceby (1993) the W–WO_2 buffer should yield a slightly higher oxygen fugacity than Fe–FeO at 800 °C and 26.1 kbar. This would imply that under Fe–FeO buffer conditions, metallic W should be the stable phase, whereas we observe WO_2. This means that either the electrochemical data should be slightly adjusted, or perhaps that very minor impurities stabilize WO_2. Cygan and Chou (1990) showed that the WO_2–$WO_{2.72}$ oxygen buffer provides significantly more oxidized conditions than Fe–FeO, but more reducing conditions relative to the Co–CoO buffer. Thus, the tungsten oxides we observe under more oxidizing conditions probably have compositions close to $WO_{2.72}$ (at Co–CoO and Ni–NiO) or $WO_{2.90}$ (at Re–ReO_2) in NaCl-free systems. Our experiments always contained some Na which, in the oxidation conditions between Co–CoO and Re–ReO_2, formed minor solid solutions with the tungsten oxide with approximate composition $Na_{0.14–0.17}WO_3$ (Table 3).

3.1.3. *Effect of fO_2 on the solubility of W- and Mo-oxides*

Table 1 and Fig. 2a show the effect of oxygen fugacity on the solubility of W-oxide and Mo-oxide in equilibrium with a fluid containing 5 wt% $NaCl_{equiv}$. The solubility of both oxides increases with increasing oxygen fugacity, but the magnitude of the effect is different. Mo-oxide solubility is significantly lower, but increases more rapidly with increasing oxygen fugacity as compared to that of W-oxide at 2.61 GPa and 800 °C (Fig. 2a) in conditions buffered by Co–CoO to Re–ReO_2. Mo-oxide solubility in these PT conditions can be reproduced by the following equation:

$$\log Mo = 0.42 \log fO_2 + 3.00 \quad (1)$$

where Mo is Mo-concentration in the fluid in molality units (i.e. in mol Mo per kg water), fO_2 is the oxygen fugacity and 3.00 is a constant. This equation suggests that Mo is dissolved in the fluid phase dominantly as Mo^{6+} according to the reaction:

$$MoO_2 + H_2O + 1/2O_2 \leftrightarrow H_2MoO_4 \quad (2)$$

The exponent of 0.42 of the oxygen fugacity in Eq. (1) may imply that a small amount of Mo^{4+} coexists in the solution with Mo^{6+}, but the solution should be Mo^{6+} dominated. Ulrich and Mavrogenes (2008) have not found a clear relationship between Mo-oxide solubility and oxygen fugacity at 2 kbar 700 °C in a similar oxygen fugacity range (Fig. 2). However, the large errors in their experiments may mask the relationship between Mo-oxide solubility and oxygen fugacity (Fig. 2a).

W-oxide solubility shows a more significant increase between the Fe–FeO and the Co–CoO buffers than in more oxidizing conditions (Fig. 2a). We therefore describe W-oxide solubility by two separate equations:

$$\log W = 0.23 \log fO_2 + 2.22 \quad (3)$$

and

$$\log W = 0.08 \log fO_2 + 0.12 \quad (4)$$

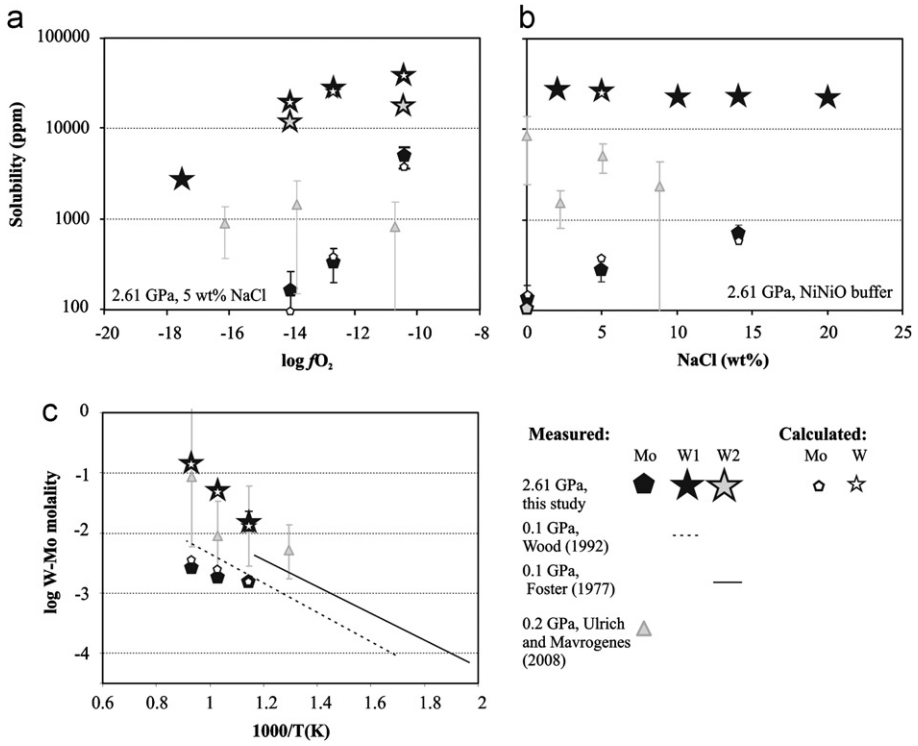

Fig. 2. Variation of W- and Mo-oxide solubility as a function of fO_2 (a), fluid salinity (b) and temperature (c). Symbols of W-oxide solubility are larger than the analytical and experimental uncertainty. W_1 refers to the solubility of tungsten oxide, W_2 to scheelite ($CaWO_4$) solubility. Open symbols are calculated concentrations based on Eqs. (8) and (9) (see text). (a) All experiments were run at 800 °C, 2.61 GPa and 5 wt% $NaCl_{equiv}$ fluid salinity. Oxygen fugacities were calculated using the equations in Frost (1991), Pownceby and O'Neill (1994), Campbell et al. (2006). (b) All experiments were run at 2.61 GPa, 800 °C in equilibrium with Ni–NiO-buffer. Gray pentagon indicates the Mo-oxide solubility in equilibrium with 5 wt% HCl. (c) All experiments were run at 2.61 GPa, 5 wt% $NaCl_{equiv}$ salinity, in equilibrium with Ni–NiO buffer. The curves for W-oxide and Ca-tungstate solubilities at 0.1 and 2.61 GPa have a similar slope, however solubilities at high pressure are significantly higher. Symbols of W-oxide solubility are larger than the analytical and experimental uncertainty. Mo-oxide solubility has a less steep slope than that of W-solubility. Comparative data for low pressure are from Wood (1992), Foster (1977) and Ulrich and Mavrogenes (2008).

where W is W-concentrations in molality units, fO_2 is the oxygen fugacity and 2.22 and 0.12 are constants. Eq. (3) is valid for fO_2 conditions between Fe–FeO and Co–CoO, whereas Eq. (4) is valid for more oxidizing conditions up to Re–ReO_2. Eq. (3) may suggest that the stoichiometry of dissolution is between the following two reactions:

$$WO_2 + H_2O + 1/2O_2 \leftrightarrow H_2WO_4 \quad (5)$$

$$WO_2 + H_2O \leftrightarrow H_2WO_3 \quad (6)$$

and the exponent of 0.23 may imply that W in these conditions dissolves in a mixed valence state of W^{4+} and W^{6+}.

At conditions between the Co–CoO and Re–ReO_2 buffers, tungsten oxide solubility depends only weakly on oxygen fugacity, which implies that there is little difference between the oxidation state of tungsten in the fluid and in the solid oxides.

Two additional experiments on the solubility of Ca-tungstate (scheelite) were carried out at 2.61 GPa (Table 1, Fig. 2a). We observed approximately 40% lower W-concentrations in these fluids as compared to those in the W-oxide solubility experiments, reflecting the lower activity of WO_3 in equilibrium with this phase. However, the scheelite data also show only a very weak dependence of solubility on oxygen fugacity.

3.1.4. Effect of fluid salinity on solubility of W- and Mo-oxides

Table 1 and Fig. 2b show the dependence of W-oxide and Mo-oxide solubility on fluid salinity. The solubility of W-oxide slightly decreases (from 27860 to 22250 ppm) with increasing fluid salinity between 2.0 and 20.0 wt% $NaCl_{equiv}$. This contrasts with some low pressure data. Wood and Vlassopoulos (1989) and Redkin and Kostromin (2010) observed at 0.1 GPa increasing W-oxide solubility with increasing fluid salinity due to the stabilization of $NaHWO_4$ or Na-bearing polymeric W-species in the fluid. On the other hand, our results agree with the theoretical calculations of Wood and Samson (2000) who have shown that the stability fields of $NaHWO_4$ and $NaWO_4^-$ are suppressed whereas that of WO_4^{2-} increased by both increasing pressure and temperature. The slight decrease of W-oxide solubility with increasing fluid salinity can be explained by the decreasing activity of H_2O.

In contrast with W, Mo-oxide solubility increases with increasing fluid salinity from 143 to 735 ppm Mo in the salinity range of 0.39 to 14.1 wt% $NaCl_{equiv}$ (Table 1, Fig. 2b). Thus the relationship between Mo-oxide solubility and fluid salinity can be described by the following equation:

$$\log Mo = 0.31 \log NaCl - 2.36 \quad (7)$$

where both Mo and Na are concentrations in the fluid in molality units. The dependence of Mo-oxide solubility on NaCl may be due to the stabilization of some chloro complexes or some alkali molybdate species in equilibrium with the hydroxy complexes. One experiment on Mo-oxide solubility in a 5 wt% HCl solution yielded a similar result as for NaCl-free fluid. This may be due to the destabilization of hydroxy complexes in a very acidic solution.

3.1.5. The effect of temperature and pressure on W- and Mo-oxide solubility

Fig. 2c shows the temperature dependence of W- and Mo-oxide solubility. Low pressure (0.1–0.2 GPa) experimental data of Wood (1992) and Ulrich and Mavrogenes (2008) are also shown for comparison. Moreover the temperature dependence of Scheelite solubility at 0.1 GPa (Foster, 1977) is also plotted. W-oxide solubility at 0.1 and 2.61 GPa have a very similar T-dependence, though the concentrations are orders of magnitude higher at 26.1 kbar. In contrast to W-oxide, there is a significant mismatch between the low and high-pressure results for Mo-oxide solubility (Fig. 2c). Mo-oxide solubility is higher at low pressure, moreover, the slope of T-dependence at low pressure is somewhat steeper than that was observed in our experiments at high pressure (Fig. 2c). The reason of discrepancy is not obvious. Our data show that Mo-oxide solubility increases much less with increasing temperature, compared to W-oxide solubility (Fig. 2c).

Combining the temperature, salinity and fO_2 dependence of Mo-oxide and W-oxide solubility at 2.61 GPa our dataset can be best fitted by the following equations:

$$\log Mo = 0.44 \log fO_2 + 0.42 \log NaCl - 1.80 \times 1000/T + 4.80 \quad (8)$$

and

$$\log W = 0.07 \log fO_2 - 4.72 \times 1000/T + 4.43 \quad (9)$$

where Mo, W and Na are in molalities. Eqs. (8) and (9) reproduces the measured Mo- and W-oxide solubilities within analytical uncertainty (Fig. 2, Table 1).

3.2. Solubility of W and Mo in mantle minerals

The solubility of W and Mo in mantle minerals has been studied at 1000 °C at different fO_2-conditions (Table 3). At these conditions the CMAS oxide powder recrystallized to a diopside+pyrope-rich garnet+/−spinel mineral assemblage. MoO_3 recrystallized to purple MoO_2 needles similar to those in the synthetic fluid inclusion experiments, whereas WO_2 reacted with CaO forming isometric $CaWO_4$ (scheelite) crystals. Garnet formed generally large (>100 μm) euhedral grains in finer grained diopside matrix (Fig. 1b). It was zoned and contained an inclusion-rich core and an almost inclusion-free rim (Fig. 1b). Inclusions in garnet cores were diopsides. Spinel occurred only in two of the run products forming euhedral crystals at the top part of the capsule. Garnet represents approximately 5 vol% of the experimental charge, whereas the amount of spinel in the run products was negligible. Al-contents of diopside showed a significant scatter inside one run product and garnet rims generally had a composition different from the cores (Table 3). All minerals had a 1–2 μm thick W- or Mo-rich rim (Fig. 1b and b/4), which made the LA-ICPMS analyses difficult for the relatively fine-grained diopsides. The rim likely formed upon quenching, as diopsides found as inclusions in garnet did not have these rims (Fig. 1b and b/4).

CMASTi oxide powder recrystallized to a diopside+pyrope-rich garnet+rutile±olivine mineral assemblage (Fig. 1c). The texture was similar to those observed in the CMAS experiments, although instead of pyroxene, rutile inclusions were abundant in garnet. The additional olivines and rutiles formed subhedral–euhedral crystals with a size up to 100 μm. Rutile was dispersed all over the capsule, while olivine formed few grains at the top. Ti-contents of clinopyroxenes varied between 0.42 and 1.14 wt%, whereas garnet contained 0.63 to 2.16 wt% TiO_2. Rutiles in MoO_2-saturated run were extremely rich in Mo, they contained up to 14.2 wt% of MoO_3.

Diopside inclusions in garnet cores and in the matrix were analyzed by LA-ICPMS in most run products. Only very few diopsides were large enough for analyses and the homogeneous signals were relatively short (Fig. 1b/2). At the latest after 10 s of ablation time grain boundary contamination was reached in the matrix clinopyroxenes (Fig. 1b/2). The presence or absence of grain boundary contamination in the analyses was also evaluated comparing the composition of inclusion and matrix diopsides. Generally 4–5 uncontaminated crystals were analyzed in all samples. The maximum solubility of W in diopside at 2.61 GPa and 1000 °C was ~60 ppm independent of oxygen fugacity, whereas the maximum solubility of Mo was ~40 ppm (Table 3).

Garnet and spinel contained at least an order of magnitude less W and Mo, as compared to diopside (Table 3). Most of these analyses yielded concentrations below detection limit. In those cases where a clear signal was detected, concentrations have been calculated. These data (0 to 12 ppm), however, should be regarded as estimates.

Two runs were spiked with $NaWO_4$-solution and remained undersaturated in W as expected from the W-solubilities at these conditions. In these runs, rutile contained a significant amount of WO_3 (up to 0.65 wt%). Silicate analyses, where grain boundary contamination could have been regarded minimal showed concentrations below detection limit (generally <10–20 ppm). Nevertheless, clear signals have been calculated and yielded 0–6 ppm of W (Table 3). In run W28 several large (>60 μm) diopsides formed in the top part of the capsule. Their cores contained 0–3 ppm W. All other analyses might be affected by at least a minimal contamination from grain boundaries. Because of the very low concentrations no clear difference can be established between garnets and clinopyroxenes.

These results show that in the peridotitic mantle clinopyroxene is the major host of W and Mo, unless rutile (or possibly a sulfide phase) is present. On the other hand, in eclogites rutile should have a strong influence on the mobility of both W and Mo in aqueous fluids.

4. Geological implications

4.1. Partitioning of W and Mo between fluid and mantle minerals

Our data show that the solubility of Mo and W in clinopyroxene and other minerals is independent of oxygen fugacity. Fluid/mineral partition coefficients will therefore primarily reflect the effects of fO_2 and salinity on the solubility of W- and Mo-oxides in the fluid (Figs. 2 and 3). The partitioning of W and Mo between aqueous fluid and minerals can be calculated as the ratio of the W- and Mo-solubility in the fluid over the W- and Mo-solubility in the mineral. A possible limitation of this approach is that the major element composition of aqueous fluid in equilibrium with a diopside+garnet+/−rutile assemblage is not exactly the same as in fluids equilibrated with quartz and this may affect the accuracy of calculated fluid/mineral partition coefficients. However, we suggest that this is a minor effect that can be neglected compared to the much stronger effects imposed by variations on oxygen fugacity and fluid salinity. In particular at relatively shallow depths of amphibole dehydration, which occurs at similar conditions as our experiments, the most important solute in aqueous fluids in equilibrium with a mantle assemblage is silica, with other components being subordinate (e.g. Kessel et al., 2005, Dvir et al., 2011). As eclogites often contain small amounts of free silica (as quartz or coesite), our fluid compositions in equilibrium with pure quartz should therefore be realistic for a dehydrating slab near the conditions of amphibole breakdown. Moreover, O'Neill and Eggins (2002) and O'Neill et al. (2008) have shown that Mo- and W-solubility in silicate melts is generally independent of melt composition, suggesting that neither of them would form complexes with components of silicate melts and both metals are dissolved as oxides. The only exception was the CaO-content of the melt. However, the mole fraction of CaO in aqueous fluids in equilibrium with an eclogitic or peridotitic assemblage is known to be very small, around 0.00–0.03 depending on temperature (e.g. Kessel et al., 2005; Dvir et al., 2011). This amount of dissolved CaO cannot introduce a significant difference in either Mo-oxide or W-oxide solubility relative to our CaO-free fluid in equilibrium with quartz. Similarly, although pH was not strictly buffered in our experiments, it is expected to be similar to the pH of upper mantle fluids. These fluids are in equilibrium with the magnesium silicate minerals of the upper mantle and of the subducted slab, which can be considered to be salts of the weak base MgO and the very weak acid SiO_2. They should therefore impose a nearly neutral to slightly alkaline pH on percolating fluids. A neutral to slightly alkaline pH is also expected for the aqueous solutions we studied, as the reduced dissociation of HCl at high temperature (Frantz and Marshall, 1984) is expected to produce a slightly alkaline reaction of NaCl solutions.

Table 4 contains the fluid/mineral partition coefficients of Mo and W at 2.6 GPa and 1000 °C, at variable fO_2 conditions and fluid salinities. First we calculated the composition of Mo- and W-saturated fluid at 1000 °C based on Eqs. (8) and (9) for fO_2 conditions between Co–CoO and Re–ReO_2 and different salinities in case of Mo. At these pressure and temperatures, NaCl-free, Mo-oxide saturated fluid contains 1400 to 43060 ppm Mo. As W-oxide was transformed to Ca-tungstate in presence of CMAS oxide powder, fluid compositions in equilibrium with Ca-tungstate had to be determined. The temperature dependence of Ca-tungstate

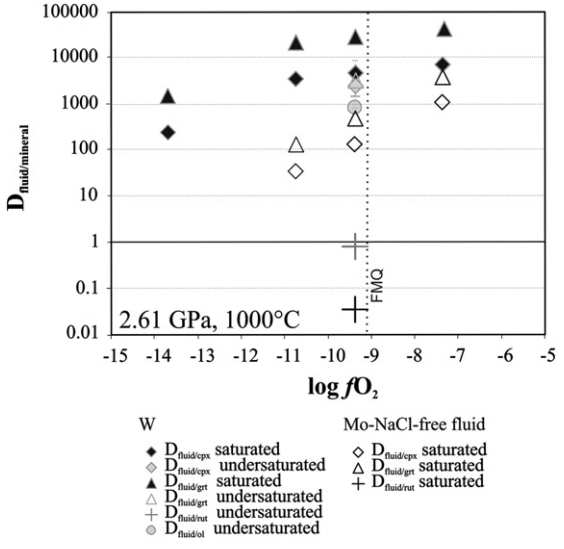

Fig. 3. Partition coefficients of W and Mo between diopside (cpx), pyrope (grt), rutile (rut) and aqueous fluid as a function of fO_2 at 2.61 GPa and 1000 °C. Partition coefficients for garnet should be regarded as minimum values (see text).

Table 4
Fluid/mineral partition coefficients of W and Mo at 1000 °C, 26.1 kbar, buffered by Fe–FeO, Co–CoO, Ni–NiO and Re–ReO_2.

	Fe–FeO	Co–CoO	Ni–NiO	Re–ReO_2
D^W-NaCl-free fluid				
Fluid/cpx saturated	240	3395	4450	6870
Fluid/cpx undersaturated	–	–	1444- > 4330	–
Fluid/garnet saturated	> 1440	> 20370	> 26690	> 41200
Fluid/garnet undersaturated	–	–	780–8520	–
Fluid/rutile undersaturated	–	–	0.8	–
Fluid/olivine undersaturated	–	–	890[b]	–
D^{Mo}-NaCl-free fluid				
Fluid/cpx saturated	–	35	137	1076
Fluid/garnet saturated	–	> 117	> 457	> 3590
Fluid/rutile saturated	–	0.011[a]	0.0374	0.293[a]
D^{Mo}-15 wt% $NaCl_{equiv}$				
Fluid/cpx saturated	–	197	788	7510
Fluid/garnet saturated	–	> 657	> 2630	> 25040
Fluid/rutile saturated	–	0.05[a]	0.21	2.05[a]

Cpx-clinopyroxene.

[a] Estimated partition coefficients assuming that Mo incorporation to rutile structure does not change with changing fO_2.

[b] Calculated based on only 1 analysis.

solubility has not been studied here, but at low pressure it shows a very similar slope to that was observed for W-oxide (Fig. 2c). Therefore we applied the relationship determined for W-oxide at high pressure, correcting for the approximately 40% lower solubility of Ca-tungstate, relative to W-oxide (Fig. 2a, Table 1). This correction factor implies a constant difference between the chemical potential of WO_3 in the pure phase and in $CaWO_4$, consistent with the solubility data. Ca-tungstate saturated aqueous fluid contains 20.36 to 41.19 wt% W at 1000 °C in the fO_2-range between the Co–CoO and Re–ReO_2 buffers. The fO_2-dependence of $D_{Mo}^{fluid/mineral}$ and $D_{W}^{fluid/mineral}$ is shown in Fig. 3. Fluid garnet partition coefficients can be regarded as minimum values as the maximum solubility of Mo and W in garnet has a quite high uncertainty (see above).

Both Mo and W are incompatible in all studied silicate minerals (Fig. 3). $D_{Mo}^{fluid/cpx}$ ranges from 35 to 1080 whereas $D_{W}^{fluid/cpx}$ varies between 3400 and 6870 at conditions between the Co–CoO and Re–ReO_2 buffers. At the Fe–FeO buffer $D_{W}^{fluid/cpx}$ is still high, ~240, showing that W will be incompatible in mantle minerals even under strongly reducing conditions. These partition coefficients are comparable to those observed between silicate melt and clinopyroxene which are generally between 1000 and 10000 for W and 63 to 1000 for Mo at mantle conditions (Hill et al., 2000; Adam and Green, 2006). The similarity of fluid/mineral and melt/mineral partition coefficients of Mo and W is consistent with the experimental and natural observation that they are only weakly fractionated between silicate melts and aqueous fluids (Keppler and Wyllie, 1991; Zajacz et al., 2008).

The calculated partition coefficients for W are particularly high. This is related to the fact that W-saturated fluids have W-concentrations on the order of tens of wt%, thus these partition coefficients might not follow Henry's law. In order to evaluate this, we carried out additional experiments with a fluid containing 4940 ppm W. This concentration is approximately 30 times lower than what is expected in W-saturated fluid at the Ni–NiO buffer and 1000 °C. If the partitioning at this W-concentration is the same as for W saturation, diopsides should contain max ~1–2 ppm of *W* whereas garnets should be virtually free of W (Table 4). Clinopyroxenes contained 0–3 ppm of W which would yield similar partition coefficients ($D_{W}^{fluid/diopside} \sim 1440 \geq 4330$) to those for W saturation ($D_{W}^{fluid/diopside} \sim 4450$), implying that Henry's law is obeyed. W-concentrations in garnet were below the 10 ppm detection limit for this phase. Some very weak signals close to background may correspond to 0.6 to 6 ppm, which would imply $D_{W}^{fluid/garnet}$ between 780 and 8500. However, these data cannot be considered to be reliable.

In contrast to silicates, both W and Mo are compatible in rutile having fluid/mineral partition coefficients of 0.8 and 0.04, respectively, at the Ni–NiO buffer at 0 wt% $NaCl_{equiv}$ salinity (Table 4, Fig. 3).

Because of the higher bulk Ti-contents, rutile is a much more common accessory phase in eclogites as compared to peridotites. Rutile will have a significant effect on the fluid/eclogite bulk partition coefficients for both W and Mo at all fO_2 conditions. On the other hand fluid/mantle bulk partition coefficients for both Mo and W are high in rutile-free peridotites. This means that a fluid phase released with a particular Mo/W ratio from the subducted slab might reach the zone of partial melting without significant modification.

The temperature dependence of fluid/mineral partition coefficients was not studied here because of the sluggish grain growth below 1000 °C in the CMAS and CMASTi experiments. Some variation of partition coefficients with either pressure or temperature cannot be ruled out. However, the currently available dataset for other trace elements suggests that a variation in pressure and temperature in the range of 3 to 6 GPa and 1000 to 1200 °C does not fundamentally change fluid/mineral partitioning (see e.g.: Stalder et al., 1998, Brenan et al., 1995).

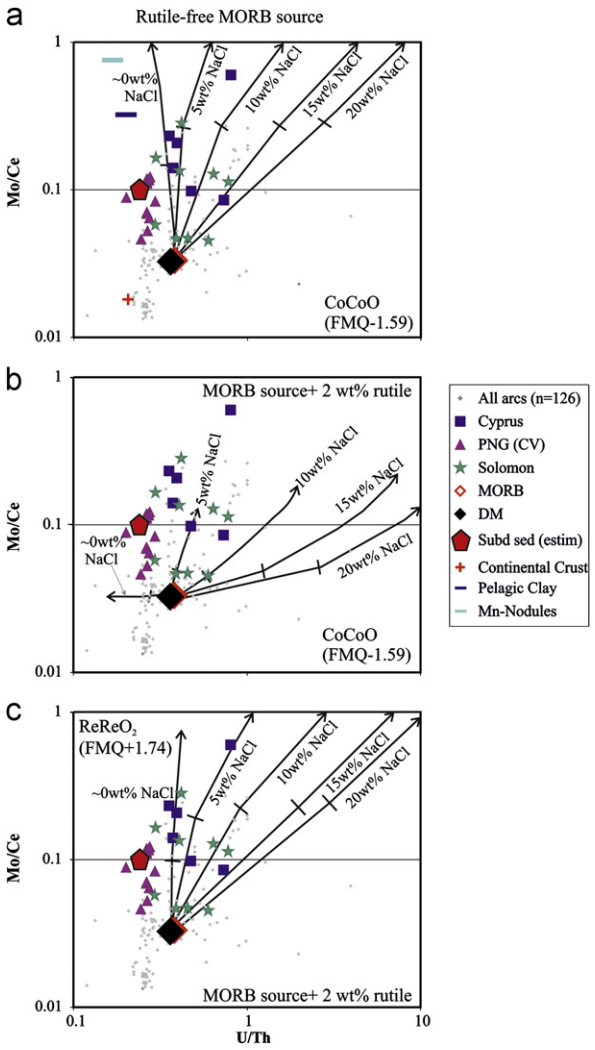

Fig. 4. Relationship between Mo/Ce and U/Th distribution in various sets of primitive arc magmas. Data source is the GEOROC database at http://georoc.mpch-mainz.gwdg.de/georoc/ (for detailed references see Appendix B). In order to avoid strongly evolved and altered samples the data were filtered based on the following parameters: mg# calculated as MgO/(MgO+FeO) > 0.45; LOI < 2, SiO_2 < 55 wt%. Figures also contain the composition of depleted mantle (DM) and marine sediments, continental crust as possible source contaminants in Figure a. For simplicity only the estimated subducted sediment composition is included in Figure b and c. U, Th, Ce contents of subducted sediment is GLOSS of Plank and Langmuir (1998). W and Mo contents of subducted sediment were estimated following the suggestion of Plank and Langmuir (1998) as composed of 76 wt% terrigenous sediment (Upper Continental Crust–Rudnick and Gao, 2004) +17 wt% of pelagic sediment (pelagic clay–Li, 1991) +7wt% of mineral bound water (assumed not to contain W and Mo). For references, see chapter 4.2. Arrows indicate mixing lines between depleted mantle and aqueous fluid released from N-MORB eclogite. The hypothetic eclogite had N-MORB composition; a garnet to cpx ratio of 30:70; and contained 0, or 2 wt% of rutile. The released fluid had a salinity of 0 to 20 wt% $NaCl_{equiv}$. Fluid compositions are in equilibrium with the Re–ReO_2 and Co–CoO buffers, which correspond to ~FMQ+1.7 and ~FMQ−1.6 at 26.1 kbar and 1000 °C. Fluid compositions were calculated based on parameters given in Appendix C. Mixing lines were calculated as DM+0.1, 0.5, 1, 5, 10, 50, 90 wt% of fluid. Marks on mixing lines indicate fluid contribution of 1 wt%. PNG–Papua New Guinea.

4.2. U–Th–Mo–W systematics in arc magmas

In the following section we will examine the possible causes of Mo/W decoupling and variable U–Th–Mo–W systematics observed in different sets of arc lavas (Figs. 4–6). Data were collected from the GEOROC database (detailed references are in Appendix B) and added to those published by König et al. (2008, 2010, 2011). The number of primitive arc basalt analyses in the GEOROC database in which U,

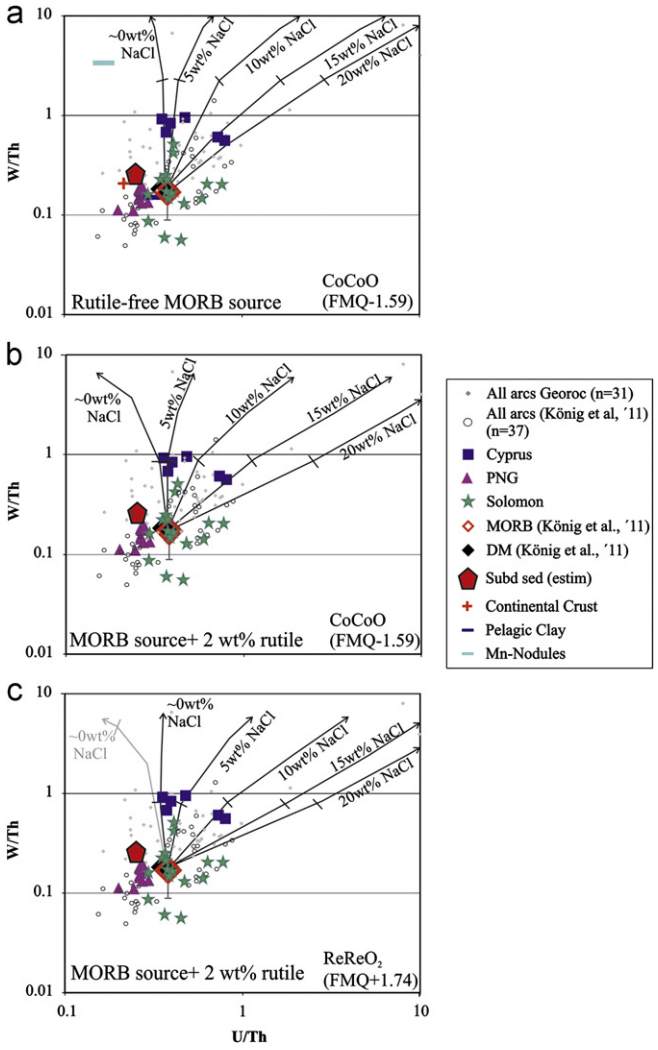

Fig. 5. Relationship between W/Th and U/Th distribution in various sets of primitive arc magmas (Appendix B). Data source, filtering parameters and mantle contaminants are the same as in Fig. 4. Grey arrow in Figure c is a mixing line between depleted mantle and subducted sediment derived fluid. Marks on mixing lines between mantle and fluid indicate fluid contribution of 1 wt%. PNG–Papua New Guinea. New high precision W-data of König et al. (2011) for variable arcs are highlighted.

Th, Mo and W were all analyzed together is very limited, so that we included all Mo data in Fig. 4 and all W data in Fig. 5.

The bulk partition coefficients of Mo and Ce, W and Th and U and Th element pairs are very similar during mantle melting (e.g.:Noll et al., 1996; Salters et al., 2002; Hill et al., 2000; Adam and Green, 2006; Arevalo and McDonough, 2008) which means that the degree of partial melting does not affect their ratios significantly. Thus, the ratio of these elements should reflect the source enrichment or depletion relative to other highly incompatible elements, including the metasomatic effects of aqueous fluids.

In addition to melt compositions, Figs. 4–6 contains the compositions of depleted mantle (Salters and Stracke, 2004 and König et al. 2011 for W) and potential subducted materials such as pelagic clay, manganese nodules (Li, 1991) and continental crust (Rudnick and Gao, 2004). These possible mantle contaminants generally cover a very narrow range in their U/Th, W/Th and Mo/Ce-ratios, the only exception being Mn-nodules. This means that Mo/Ce and W/Th ratios significantly higher than for depleted mantle, as observed in many arc lavas, cannot be explained by their contribution. Mixing between depleted mantle and continental crust might explain the lower Mo/Ce and U/Th ratios in some of the arc lavas (Fig. 4a). One can interpret this relationship as the effect of subducted sediment contribution to the source or by crustal contamination during magma evolution. We propose that as these lavas (mainly Aeolian Island samples) were erupted on a thick continental crust, crustal contamination might have overwritten the subduction contribution in terms of Mo.

Figs. 4 and 5 also show how the addition of aqueous fluid changes the Mo/Ce, W/Th and U/Th ratios of the mantle source. Fluid compositions released from the subducted slab were calculated in equilibrium with N-MORB–eclogite with or without residual rutile. The most significant fluid release in the oceanic crust is expected at the amphibolite–eclogite transition due to the reaction:

$$3\ \text{glaucophane} + 6\ \text{clinozoisite} \rightarrow 9\ \text{pyrope} + 26\ \text{jadeite} + 12\ \text{diopside} + 19\ \text{quartz} + 6H_2O \quad (10)$$

that produces ~2 wt% of fluid, and an eclogite with a garnet clinopyroxene ratio of ~30:70 (Feineman et al., 2007). Applying these mineral and fluid ratios, fluid compositions were modeled for amphibolite–eclogite transition by batch equilibrium fluid release, given by the formula:

$$C_{\text{fluid}} = C_0/(F + (1-F) \times D) \quad (11)$$

where C_{fluid} is the composition of the fluid released, C_0 is the initial concentration of the residual eclogite (N-MORB), F is the fluid fraction and D is the solid/fluid bulk partition coefficients of the residual material. Starting N-MORB and subducted sediment compositions as well as other parameters of calculations are in Appendix C.

For the modeling we used partition coefficients calculated at 1000 °C whereas amphibole dehydration takes place at lower temperatures (~800 °C). This might introduce some uncertainty in the absolute element concentrations in the model fluid composition and thus in the absolute amount of fluid which should be added to the source region of island arc magmas. However, the major systematics might only be slightly affected by this factor. Furthermore, the fluid compositions calculated in equilibrium with clinopyroxene-rich eclogite should be regarded realistic for higher pressure and temperature conditions as long as the aqueous fluid, produced e.g. by serpentine dehydration, passes through and re-equilibrates with an overlying eclogitic body. Experiments by Klimm et al. (2008) showed that residual allanite in eclogites is also capable of fractionating U from Th. They have also demonstrated that both elements are very strongly compatible in allanite. However, the fluid/mineral partition coefficients determined by Bali et al. (2011) can reproduce the large U-excess observed in arc lavas without invoking the additional presence of accessory allanite.

According to these calculations W/Th ratios in the melt will only depend on the residual rutile content of the subducted material and the fluid fraction in the source of melting (Fig. 5). In contrast, Mo/Ce, U/Th and Mo/W ratios will depend on oxygen fugacity, fluid salinity and the residual rutile content in the eclogite and the fluid content in the region of melting (Figs. 4 and 6). In general W/Th vs. U/Th ratios in all melt compositions plotted in Fig. 6 can be modeled by mixing of depleted mantle and a 1–2 wt% of aqueous fluid originated from subducted MORB or sediment. The rutile content in residual eclogite generally does not have to be more than 2–3 wt%, and fluid salinity does not have to be higher than 20 wt% $NaCl_{equiv}$. Similar relationship is seen in the Mo/Ce vs. U/Th diagrams (Fig. 4). However, increasing rutile content in the MORB eclogite decreases significantly the Mo/Ce ratios of the fluid in reduced conditions (Fig. 4b). The aqueous fluid will be too poor in Mo to be responsible for the highest Mo/Ce ratios in e.g. Cyprus boninites. Thus, we need to determine the rutile content of the residual eclogite by independent element ratios and all remaining parameters can be calculated.

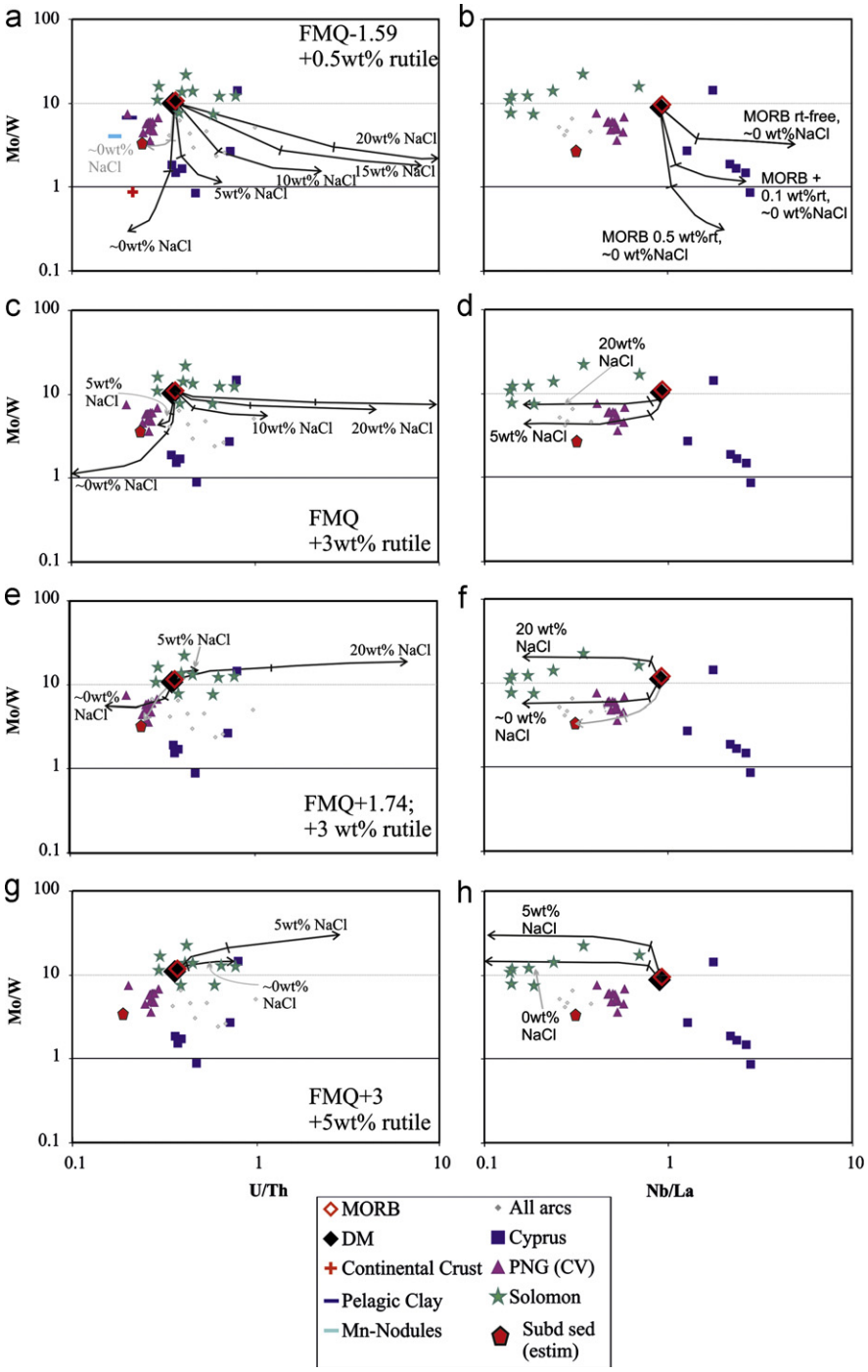

Fig. 6. Relationship between Mo/W–U/Th (a, c, e, and g) and Nb/La (b, d, f, and h) distribution in Cyprus and Papua New Guinea (PNG) boninites, Solomon island (König et al. 2008, 2010) and other (Bolge et al., 2006; Dosseto et al., 2003; Duggen et al., 2007) arc basalts. Fluid compositions were calculated based on the parameters listed in Appendix C for variable fO_2 and rutile content in the residual eclogite. Black arrows are mixing lines between depleted mantle and hypothetic fluids. Grey arrow: in Figure a–mixing line for a rutile-free source; in Figure e and f–mixing line between depleted mantle and subducted sediment. Note the strong dependence of Mo/W ratios on fO_2 and Nb/La on rutile content in residual eclogite.

The Nb/La-ratios can be a good proxy for the modal abundance of rutile content in the residual eclogite, as Nb is strongly compatible in rutile upon fluid release (Brenan et al., 1994; Stalder et al., 1998). Nb/La ratios of Cyprus and Papua New Guinea (PNG) boninites and Solomon Island arc lavas strongly differ from each other (Fig. 6). Cyprus boninites have Nb/La ratios which are higher than MORB. This can only be achieved if the residual eclogite contained max. 0.5 wt% rutile. Thus, Mo/W and Mo/Ce ratios of these melts can be modeled by the addition of a 1–2 wt% of relatively reduced ($\sim$FMQ-1.5), low salinity (<5 wt%) fluid to depleted mantle.

König et al. (2008) suggested that the source region of PNG boninites was strongly contaminated by subducted pelagic sediments (see also Fig. 4 and Fig. 6e). W/Th ratios of these volcanites are similar or lower than those of MORB and subducted sediment (Fig. 5). Low W/Th coupled with low U/Th ratios were observed in other arc lavas with high subducted sediment influence too (König et al. (2011); Fig. 5). The simple addition of sediment melt component explains only the low U/Th ratios in these melts (see Nebel et al., 2010). However, if we assume that the metasedimentary (or MORB) eclogite has previously been leached by

aqueous fluid, which removed significant amount of W and U from the rock, the leached residuum should have lower W/Th and U/Th ratios than MORB. Subsequent melting of this material will produce a metasomatic melt with low W/Th and U/Th ratios.

Solomon Island arc lavas have the highest Mo/W and the lowest, but highly variable Nb/La in Fig. 6. The low Nb/La ratios suggest that the residual eclogite was relatively rutile-rich (≥ 5 wt). In Fig. 5 two separate series can be distinguished, one with increasing W/Th ratios at a relatively constant and low U/Th, and another with an increasing U/Th at a relatively constant but low W/Th. The first series requires a low salinity fluid released from relatively oxidized source ($\sim$FMQ+2–3, 0–5 wt% $NaCl_{equiv}$) whereas a higher salinity fluid could have contributed to the source of the second series. All these are in accordance with the discussion of König et al. (2008, 2010) on the origin of these arc lavas.

Thus we suggest that keeping in mind all geochemical signatures that determine the metasomatic material (e.g. MORB melt, sediment melt vs. aqueous fluid) in the region of melting the Mo–W–U–Th systematics of arc lavas can be an effective tool to estimate both fO_2 and fluid salinity as well as the amount of aqueous fluid in the source of arc magmas.

5. Conclusions

We have studied the mobility of W and Mo in aqueous fluid in the mantle. The solubility of W-oxide is insensitive to oxygen fugacity whereas Mo-oxide solubility is strongly dependent on oxygen fugacity. The Mo/W ratio is therefore a sensitive indicator of redox conditions in subduction zones. At mantle conditions fluid salinity does not affect W-oxide solubility, whereas Mo-oxide solubility increases with fluid salinity. Oxygen fugacity does not have any effect on the incorporation mechanism of either W or Mo in mantle minerals, thus fluid/mineral partition coefficients reflect the fO_2-dependence of W and Mo solubility in the fluid. Both W and Mo are incompatible in silicate minerals in the presence of aqueous fluid in mantle conditions, but both of them are compatible in rutile. The Mo–W–U–Th systematics of arc magmas tightly constrains the amount and salinity of the slab fluid as well as the redox conditions during dehydration. Provided that the modal abundance of rutile is independently constrained, W/Th ratios are particularly useful tracers for the amount of slab fluid released into the mantle wedge.

Acknowledgments

The paper benefited from constructive reviews of Stephan König (University of Bonn) and an anonymous reviewer and the helpful editorial handling of Tim Elliott (University of Bristol).

Appendix A. Supporting information

Supplementary data associated with this article can be found in the online version at http://dx.doi.org/10.1016/j.epsl.2012.07.032.

References

Adam, J., Green, T., 2006. Trace element partitioning between mica- and amphibole-bearing garnet lherzolite and hydrous basanitic melt: 1. Experimental results and the investigation of controls on partitioning behavior. Contrib. Mineral. Petrol. 152, 1–17.

Arevalo, R., McDonough, W.F., 2008. Tungsten geochemistry and implications for understanding the Earth's interior. Earth Planet. Sci. Lett. 272, 656–665.

Bali, E., Audetat, A., Keppler, H., 2011. The mobility of U and Th in subduction zone fluids—an indicator of oxygen fugacity and fluid salinity. Contrib. Mineral. Petrol. 161, 597–613.

Bolge, L.L., Carr, M.J., Feigenson, M.D., Alvarado, G.E., 2006. Geochemical stratigraphy and magmatic evolution at Arenal Volcano, Costa Rica. J. Volcanol. Geotherm. Res. 157, 34–48.

Brenan, J.M., Shaw, H.F., Phinney, D.L., Ryerson, F.J., 1994. Rutile-aqueous fluid partitioning of Nb, Ta, Hf, Zr, U and Th: implications for high field strength element depletions in island-arc basalts. Earth Planet. Sci. Lett. 128, 327–339.

Brenan, J.M., Shaw, H.F., Ryerson, F.J., Phinney, D.L., 1995. Mineral-aqueous fluid partitioning of trace elements at 900 °C and 2.0 GPa: Constraints on the trace element chemistry of mantle and deep crustal fluids. Geochim. Cosmochim. Acta 59, 3331–3350.

Cygan, G.L., Chou, I.M., 1990. The assemblage WO_2+H_2O as a steady-state hydrogen source in moderately reduced hydrothermal experiments. Am. Mineral. 75, 1399–1405.

Campbell, A.J., Danielson, L., Righter, K., Wang, Y., Davidson, G., 2006. Oxygen fugacity at high pressure:equations of state of metal-oxide pairs. Lunar and Planetary Science. XXXVII Abstract #1977.

Dosetto, A., Bourdon, B., Joron, J-L., Dupre, B., 2003. U–Th–Pa–Ra study of the Kamchatka Arc: new constraints on the genesis of arc lavas. Geochim. Cosmochim. Acta 67, 2857–2877.

Duggen, S., Portnyagin, M.V., Baker, J.A., Ulfbeck, D.G., Hoernle, K., Garbe-Schönberg, C.D., Grassineau, N., 2007. Drastic shift in lava geochemistry in the volcanic-front to rear-arc region of the Southern Kamchatkan subduction zone: evidence for the transition from slab surface dehydration to sediment melting. Geochim. Cosmochim. Acta 71, 452–480.

Dvir, O., Pettke, T., Fumagalli, P., Kessel, R., 2011. Fluids in the peridotite–water system up to 6 GPa and 800 °C: new experimental constrains on dehydration reactions. Contrib. Mineral. Petrol. 157, 829–844.

Feineman, M.D., Ryerson, F.J., DePaolo, D.J., Plank, T., 2007. Zoisite-aqueous fluid trace element partitioning with implications for subduction zone fluid composition. Chem. Geol. 239, 250–265.

Foster, R.P., 1977. Solubility of Scheelite in hydrothermal chloride solutions. Chem. Geol. 20, 27–43.

Frantz, J.D., Marshall, W.L., 1984. Electrical conductances and ionization constants of salts, acids, and bases in supercritical aqueous fluid: I. Hydrochloric acid from 100 °C to 700 °C and at pressures to 4000 bar. Am. J. Sci. 284, 651–667.

Frost, B.R., 1991. Introduction to oxygen fugacity and its petrologic importance. In: Lindsley, D.H. (Ed.), Oxide Minerals: Petrologic and Magnetic Significance. Reviews in Mineralogy, pp. 1–9.

Greenwood, N.N., Earnshaw, A., 1984. Chemistry of the elements. Pergamon Press, Oxford.

Guillong, M., Heinrich, C.A., 2007. Sensitivity enhancement in laser ablation ICP–MS using small amounts of hydrogen in the carrier gas. J. Anal. At. Spectrom. 12, 1488–1494.

Hill, E., Wood, B.J., Blundy, J.D., 2000. The effect of Ca-Tschermaks component on trace element partitioning between clinopyroxene and silicate melt. Lithos 53, 203–215.

Jacobsen, S.B., Harper Jr., C.L., 1995. Accretion and early differentiation history of the Earth based on extinct radionuclides. In: Basu, A.R., Hart, S.R. (Eds.), Isotopic Studies of Crust–Mantle Evolution. American Geophysical Union, Washington, DC.

Keppler, H., Wyllie, P.J., 1991. Partitioning of Cu, Sn, Mo, W, U, and Th between melt and aqueous fluid in the systems haplogranite–H_2O–HCl and haplogranite–H_2O–HF. Contrib. Mineral. Petrol. 109, 139–150.

Kessel, R., Schmidt, M., Ulmer, P., Pettke, T., 2005. Trace element signature of subduction-zone fluids, melts and supercritical liquids at 120–180 km depth. Nature 437, 724–727.

Klimm, K., Blundy, J.D., Green, T.H., 2008. Trace element partitioning and accessory phase saturation during H_2O-saturated melting of basalt with implications for subduction zone chemical fluxes. J. Petrol. 49, 523–553.

König, S., Münker, C., Schuth, S., Garbe-Schönberg, D., 2008. Mobility of tungsten in subduction zones. Earth Planet. Sci. Lett. 274, 82–92.

König, S., Münker, C., Schuth, S., Luguet, A., Hoffmann, J.E., Kuduon, J., 2010. Boninites as windows into trace element mobility in subduction zones. Geochim. Cosmochim. Acta 74, 684–704.

König, S., Münker, C., Hohl, S., Paulick, H., Barth, AR., Lagos, M., Pfander, J., Bühl, A., 2011. The Earth's tungsten budget during mantle melting and crust formation. Geochim. Cosmochim. Acta 75, 2119–2136.

Labbe, P., 1992. Tungsten oxides, tungsten bronzes and tungsten bronze type structures. Key Eng. Mater. 68, 293–339.

Lee, D.C., Halliday, A.N., 1995. Hafnium–tungsten chronometry and the timing of terrestrial core formation. Nature 378, 771–774.

Li, Y.H., 1991. Distribution patterns of the elements in the ocean–a synthesis. Geochim. Cosmochim. Acta 55, 3223–3240.

Nebel, O., Vroon, P.Z., Viggers de Vires, D.F., Jenner, F.E., Mavrogenes, J.A., 2010. Tungsten isotopes as tracers of core–mantle interactions: the influence of subducted sediments. Geochim. Cosmochim. Acta 74, 751–762.

Noll, P.D., Newsom, H.E., Leeman, W.P., Ryan, J.G., 1996. The role of hydrothermal fluids in the production of subduction zone magmas: evidence from siderophile and chalcophile trace elements and boron. Geochim. Cosmochim. Acta 60, 587–611.

O'Neill, H.St.C., Berry, A.J., Eggins, S.M., 2008. The solubility and oxidation state of tungsten in silicate melts: Implications for the comparative chemistry of W and Mo in planetary differentiation processes. Chem. Geol. 255, 346–359.

O'Neill, H.St.C., Eggins, S.M., 2002. The effect of melt composition on trace element partitioning: an experimental investigation of the activity coefficients of FeO, NiO, CoO, MoO_2 and MoO_3 in silicate melts. Chem. Geol. 186, 151–181.

O'Neill, H.St.C., Pownceby, M.I., 1993. Thermodynamic data from redox reactions at high temperatures. I. An experimental and theoretical assessment of the

electrochemical method using stabilized zirconia electrolytes, with revised values for the Fe–FeO, Co–CoO, Ni–NiO and Cu–CuzO oxygen buffers, and new data for the W–WO_2 buffer. Contrib. Mineral. Petrol. 114, 296–314.

Plank, T., Langmuir, C.H., 1998. The geochemical composition of subducting sediment and its consequences for the crust and mantle. Chem. Geol. 145, 325–394.

Pownceby, M.I., O'Neill, H.St.C., 1994. Thermodynamic data from redox reactions at high temperatures. IV. Calibration of the Re–ReO_2 oxygen buffer from EMF and NiO+Ni–Pd redox sensor measurements. Contrib. Mineral. Petrol. 118, 130–137.

Redkin, A.F., Kostromin, N.P., 2010. On the problem of transport species of tungsten by hydrothermal solutions. Geochem Int. 48, 988–998.

Rudnick, R.L., Gao, S., 2004. Composition of the continental crust. In: Holland, H.D., Turekian, K.K. (Eds.), Treatise on Geochemistry, The Crust, 3. Elsevier, Amsterdam, pp. 1–64.

Salters, V.J.M., Longhi, J.E., Bizimis, M., 2002. Near mantle solidus trace element partitioning at pressures up to 3–4 GPa. G-Cubed, 3, , http://dx.doi.org/10.1029/2001GC000148.

Salters, V., Stracke, A., 2004. Composition of the depleted mantle. G-Cubed 5 , http://dx.doi.org/10.1029/2003GC000597, Q05B07, 27p..

Seo, J.H., Guillong, M., Aerts, M., Zajacz, Z., Heinrich, C.A., 2011. Microanalysis of S, Cl, Br in fluid inclusions by LA-ICP-MS. Chem. Geol. 284, 35–44.

Stalder, R., Foley, S.F., Brey, G.P., Horn, I., 1998. Mineral aqueous fluid partitioning of trace elements at 900–1200 °C and 3.0–5.7 GPa: new experimental data for garnet, clinopyroxene, and rutile, and implications for mantle metasomatism. Geochim. Cosmochim. Acta 62, 1781–1801.

Ulrich, T., Mavrogenes, J., 2008. An experimental study of the solubility of molybdenum in H_2O and KCl–H_2O solutions from 500 °C to 800 °C, and 150 to 300 MPa. Geochim. Cosmochim. Acta 72, 2316–2330.

Wood, S.A., Samson, I.M., 2000. The hydtothermal geochemistry of tungsten in granitoid environments: I relative solubilities of Ferberite and Scheelite as a function of T, P, pH, and m_{NaCl}. Econ. Geol. 95, 143–182.

Wood, S.A., Vlassopoulos, D., 1989. Experimental determination of the hydrothermal solubility and speciation of tungsten at 500 °C and 1 kbar. Geochim. Cosmochim. Acta 53, 303–312.

Wood, S.A., 1992. Experimental determination of the solubility of WO_3(s) and the thermodynamic properties of H_2WO_3(aq) in the range 300–600 °C at 1 kbar: calculation of scheelite solubility. Geochim Cosmochim Acta 56, 1827–1836.

Zajacz, Z., Halter, W.E., Pettke, T., Guillong, M., 2008. Determination of fluid/melt partition coefficientsby LA-ICPMS analysis of co-existing fluid and silicate melt inclusions: Controls on element partitioning. Geochim. Cosmochim. Acta 72, 2169–2197.